Influence of sputter pressure on magnetic and structural properties of Permalloy thin films

Singh, Sukhvinder ; Abelmann, Leon; Gao, Haibin ; Hartmann, Uwe

DOI
10.1016/j.jmmm.2023.171138

Publication date
2023

Document Version
Final published version

Published in
Journal of Magnetism and Magnetic Materials

Journal of Magnetism and Magnetic Materials 586 (2023) 171138

Contents lists available at ScienceDirect

Journal of Magnetism and Magnetic Materials

journal homepage: www.elsevier.com/locate/jmmm

Research article

Influence of sputter pressure on magnetic and structural properties of Permalloy thin films

Sukhvinder Singh [a,*], Leon Abelmann [b,c], Haibin Gao [a], Uwe Hartmann [a]

[a] Institute of Experimental Physics, Saarland University, 66123, Saarbrücken, Germany
[b] Korea Institute of Science and Technology (KIST) Europe, 66123, Saarbrücken, Germany
[c] Electrical Engineering, Mathematics and Computer Science (EEMCS), Delft University of Technology, 2628 CD, Delft, The Netherlands

ARTICLE INFO

Keywords:
Permalloy
Magnetic domains
Sputtering
Magnetic force microscopy

ABSTRACT

Well-defined and technically relevant domain configurations are sought in patterned magnetic thin films. We used Magnetic Force Microscopy to investigate these in square-patterned Permalloy films. The films were prepared using dc sputter deposition by varying the Argon pressure from 1.5×10^{-3} to 30.0×10^{-3} mbar. The Landau domain configuration was found in films prepared at 1.5×10^{-3} mbar pressure. With an increase in pressure, tulip and irregular domains were consecutively formed. Based on magnetic and structural characterizations, an increase in coercivity and a decrease in Permalloy film density were observed at the same time.

1. Introduction

Well-defined, stable and reproducible magnetic domain configurations are required for various devices based on magnetic thin films [1–4]. However, even for a given geometry, patterned films often show more than one domain configuration in their zero-field states [5–9]. Some of these zero-field states show complex domain configurations which are undesirable from the application point of view [10–14]. The Landau domain configuration [15,16] is one of the simple and technically important [2,3,17] zero-field states, which exist in square-patterned magnetic films above a particular film thickness [15,18]. In the Landau configuration, four triangular closure domains keep the magnetic flux almost completely within the structure. The four-fold magnetic symmetry results in the formation of a single vortex in the center of the structure [17,19]. However, apart from the Landau domain configuration, square-patterned films also show tulip [20,21], diamond [5,22] or irregular domain configurations [10–13] in the absence of external fields. Zero-field domain configurations are determined by various structural properties such as geometry [5,15,20], intrinsic stress [10,14,23], grain morphology [22,24–27] as well as direction and strength of a magnetic field possibly applied during the fabrication processes [10,20,28]. Moreover, due to influences of the magnetic history [29] such as trapped vortices from previous reversals [30,31] and because of the changes of energy landscapes with the variation of magnetization sweep rate [6,7,9], often some of the higher energy states stabilize instead of the ground state. These excited states are then metastable ones.

Permalloy (Py) with a $Ni_{80}Fe_{20}$ composition is a frequently used magnetic material for both basic research and technical applications [32] because of its negligibly small magneto-crystalline anisotropy and almost vanishing magnetostriction coefficient [33,34]. Due to the soft magnetic properties of Py films, their domain configurations are mainly defined by the shape and dimensions of a given pattern [20,35]. However, with the deviation of the structural characteristics from their ideal bulk characteristics [34], the soft magnetic properties of the Py films easily deteriorate due to the development of an anisotropy resulting from the grain morphology [36,37] and/or from the stress in conjunction with a non-zero magnetostriction of the films [14,38,39]. This results in an increase of the number of energy contributions which determine the magnetic properties of the films [20]. This in turn leads to an increase in complexity of the observed ground-state domain configurations [10,14,40].

The structural characteristics of the films depend on the chosen deposition method. Out of the various thin-film-deposition techniques, sputter deposition allows adjustability of a number of parameters in order to achieve the desired quality of a film for various materials [41–43]. The composition, uniformity, adhesion strength, stress, and grain morphology of the film can be controlled by optimizing the substrate bias voltage [44–47], buffer layers at the film–substrate interface [48,49], substrate heating [45,50], sputter power [44,47], substrate-to-target distance [42,43,51], and Argon (Ar) pressure [52–54] during the sputter deposition. Especially, by varying the Ar pressure, crucial

* Corresponding author.
E-mail address: s.singh@mx.uni-saarland.de (S. Singh).

https://doi.org/10.1016/j.jmmm.2023.171138
Received 18 April 2023; Received in revised form 3 July 2023; Accepted 10 August 2023
Available online 21 August 2023

deposition parameters such as the flux rate, composition, angular incidence distribution of sputtered atoms [55,56], and adsorption to the substrate can be controlled [53,54,57]. Py films become magnetically harder [46,52,54] and their surface roughness increases upon increase of the Ar pressure [52,54]. Both these effects lead to the increase in domain wall pinning site strength [58–60]. One may expect that at too high pressure the movement of domain walls and consequently the domain configurations are affected by the granular structure of the films. Above that pressure, we expect that the Landau domain configuration can no longer be attained. In this report we investigate at what pressure this happens, and what are the related values for chemical composition, morphology, and texture to achieve Landau domain configuration reliably.

2. Experimental and computational details

Continuous and patterned Py films were prepared by dc magnetron sputtering. P-type Si(100) substrates of 525 ± 20 μm thickness were first cleaned in an ultrasonic bath in acetone and isopropanol solutions, and later washed with de-ionized water and dried in a N_2 gas flow, respectively. No oxide removal method was used during sample preparation. To prepare patterned samples, the cleaned Si substrates were spin-coated by PMMA (Poly(methyl methacrylate)) layers. The PMMA-coated substrates were patterned using e-beam lithography. The pattern consists in arrays of 5 × 5 μm^2 squares having 10 μm edge-to-edge interspacing. A Py target of composition $Ni_{80}Fe_{20}$ and a diameter of 5 cm was used for all depositions. The uncooled substrates of 5 mm edge lengths were placed at a distance of 11 cm from the target. The base pressure in the sputter chamber was 6.0×10^{-6} mbar. Different depositions were performed setting the Ar pressure to 1.5×10^{-3}, 5.0×10^{-3}, 7.0×10^{-3}, and 30.0×10^{-3} mbar, respectively. No magnetic field was applied during sputtering. The dc power was kept approximately at 104 Watt. The films were deposited with thicknesses between 50 nm and 70 nm. No capping layer was deposited. After the deposition, a lift-off process was performed in acetone, and the samples were finally cleaned in de-ionized water.

Structural and magnetic investigations were carried out on both continuous and patterned Py film samples. Grazing Incidence X-ray Diffraction (GIXRD) analysis of the films was performed by a PANalytical X'Pert MRD diffractometer with CuKα radiation (λ = 0.15406 nm) operating at 40 kV and 40 mA, at 0.42° incidence angle. The cross-sectional morphology of the continuous Py films was examined with a JEOL JEM2011 Transmission Electron Microscope (TEM) and JEOL ARM200F Scanning Transmission Electron Microscope (STEM). The topography was analyzed with a Veeco Multimode Atomic/Magnetic Force Microscope (AFM/MFM). The elemental composition of the Py films was investigated with a Genesis 2000 energy-dispersive X-ray (EDX) spectroscope. For the magnetic measurements, the in-plane and out-of-plane magnetic hysteresis loops of the continuous films were measured with a DMS model 10 vector Vibrating Sample Magnetometer (VSM). The sample size was 5×5 mm^2. The system was calibrated with a 0.3 mm thick Ni foil of an identical area and a weight of 60.1 mg, which we assumed has a moment of 3.31 mAm^2 using literature value for the saturation magnetization of Ni (55.1 Am^2kg^{-1}) [61]. The diamagnetic contribution of the sample holder and the Si substrate was subtracted by a linear background signal of 0.2 μAm^2T^{-1}, obtained by a fit to the high field branches of the in-plane hysteresis loops. The component of the magnetic moment perpendicular to the field was negligible for all measurements and was ignored. The magnetic moment was converted to magnetization using the film thickness obtained by the TEM, and the area of the samples obtained by ImageJ software [62]. The magnetic domain configurations of the patterned Py films were analyzed with the MFM mentioned above.

The energies of the different types of domain configurations in a Py square were micromagnetically calculated. The Object Oriented Micro-Magnetic Framework (OOMMF) [63] with a cubic cell of 10 nm edge length was used to perform the three-dimensional simulations. We assumed a saturation magnetization of $M_s = 860 \times 10^3$ Am^{-1} [32,64], an exchange constant of $A = 13 \times 10^{-12}$ Jm^{-1} [64,65], and Gilbert gyromagnetic ratio $\gamma_G = \mu_o \gamma_e = 2.21 \times 10^5$ $m(As)^{-1}$, where μ_o is the vacuum permeability constant and γ_e is the free electron gyromagnetic ratio. To perform the static simulations, a damping parameter of $\alpha = 0.5$ was applied [64]. The convergence criterion $|\mathbf{M} \times \mathbf{H}| / M_s^2 \leq 1 \times 10^{-5}$ as a torque minimization condition was employed in the calculations.

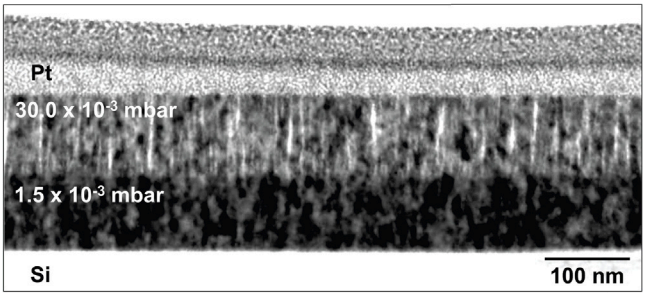

Fig. 1. Bright-field TEM image of the cross-sectional morphology of the Py films grown consecutively on a Si substrate at 1.5×10^{-3} and 30.0×10^{-3} mbar Ar pressures. A capping layer of Pt was deposited on top to protect the Py films during the necessary FIB treatment. The film deposited at 30.0×10^{-3} mbar appears lighter, which suggests a reduction in film density. Moreover, columnar structures with clear voids appear to be formed.

3. Experimental and simulation results

3.1. Morphology and crystal structure of Py films as a function of Ar pressure

Granular structure of Py films prepared at 1.5×10^{-3} and 30.0×10^{-3} mbar Ar pressures was investigated in more detail by TEM and STEM. To observe the cross-sectional morphology by TEM, a slice of both films deposited on top of each other was prepared by Ga^+ Focused Ion Beam (FIB) milling. These films were deposited on top of each other so that the TEM image could be made under exactly the same conditions (exposure and thickness of TEM slice) and comparison was possible. From the TEM analysis shown in Fig. 1, it is clearly visible that the film deposited at 1.5×10^{-3} mbar Ar pressure grew with a denser morphology, whereas the film deposited at 30.0×10^{-3} mbar shows columnar grains separated by voids. The growth of the second layer on top of the first did not alter the grain morphologies of the both films. The corresponding cross-sectional images of separately grown films are shown in the Supplementary Material (Fig. S1). An Electron Energy-Loss Spectroscopy (EELS) line profile shows an increase of O and decrease of Ni and Fe contents at the void as seen in Fig. 2. No change in the crystallite size at varying Ar pressure is observed in the TEM images. Moreover, similar to the results published by other groups [51,54], an increase of Ni content was observed in our samples with the increase of Ar pressure, as presented in the EDX data in Table 1. The respective increase of O content with the increase of Ar pressure found in the EDX data is also presented in Table 1.

Fig. 3 shows the GIXRD patterns of a bare P-type Si(100) substrate and the Py films sputtered on top of Si substrates at different Ar pressures. From Fig. 3 it is clear that with the increase of the Ar pressure, the basic crystal structure of the Py films remains unchanged, whereas almost all GIXRD peaks decrease. All Py films show a fcc phase with a preponderance of (111) crystallographic planes oriented parallel to the film surface. The crystallite size calculated by the Williamson–Hall method [66] remains in the 9–12 nm range. In our result, GIXRD analysis of a bare Si(100) substrate show peaks in 50–60° range as also reported by Refs. [67–69]. There are two sharp peaks at 51° and 53.6° and a broader peak at approximately 55.5°. For a Si(100) substrate

Table 1
Sputter parameters, structural and magnetic properties of deposited Py films. With increasing sputter pressure we observe a strong reduction in the deposition rate and magnetization, and a strong increase in the oxygen content and coercivity. The Ni concentration increases slightly.

Ar Press. ($\times 10^{-3}$ mbar)	Dep. rate (nm/min)	Thickness (nm)	Ni (Ni:Fe)[a] (at%)	O (Ni:Fe:O)[b] (at%)	$\mu_o H_c^{\text{in-plane}}$ (mT)	$M_s^{\text{film}}/M_s^{\text{bulk}}$
1.5	18.6	65	80.3	10.2	0.12	0.92
5.0	13.2	50	82.2	16.2	0.40	0.77
7.0	10.7	51	83.8	25.3	5.73	0.63
30.0	4.0	67	83.7	38.5	4.30	0.53

[a]Ni at%, considering Ni and Fe as components.
[b]O at%, considering Ni, Fe and O as components.

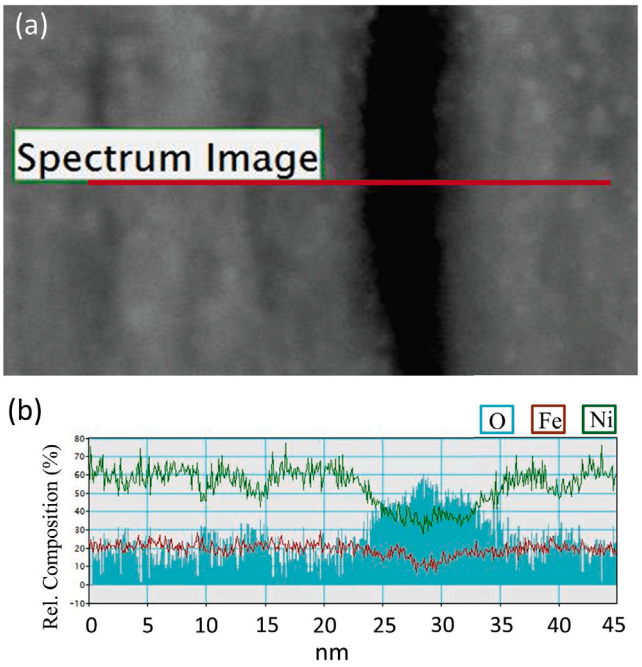

Fig. 2. (a) A cross-section of the Py film deposited at 30.0×10^{-3} mbar Argon pressure taken with a Scanning Transmission Electron Microscope in dark-field contrast. (b) A spectrum image from a 45 nm EELS line profile of a gap between columnar grains formed inside the film. This is the same sample shown in Fig. 1.

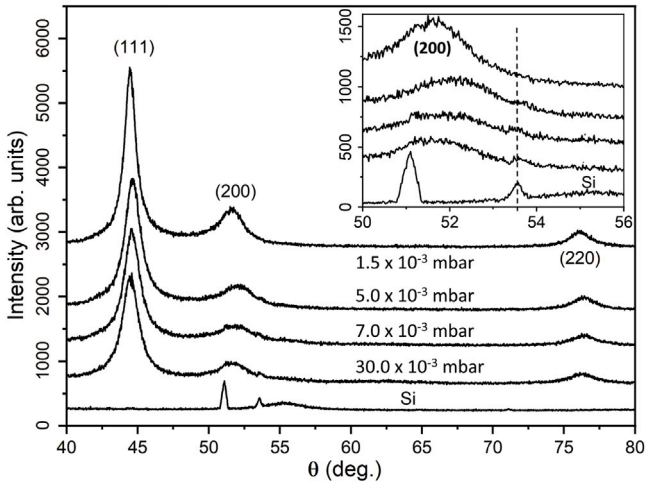

Fig. 3. GIXRD patterns of a bare Si(100) substrate and Py films deposited at different Ar pressures. The inset shows in detail the influence of the substrate on the GIXRD patterns. There is no significant change in crystal structure. At high pressure we see the influence of the substrate suggesting that the film becomes less dense.

(wafer), the (311) planes are oriented at approximately 25.2° from the substrate surface [70]. For a grazing incidence angle (omega = 0.42°) these planes fulfill the Bragg condition and therefore are observed. The (311) peak shifts towards lower angle in the 50–60° range with decrease of grazing incidence angle [67]. The peak observed at 51° is from (311) plane [67]. The other sharp peak at 53.6° is possibly from native SiO_2 layer on the Si substrate or from silicon hydrides [68, 71]. The weak broader peak at 55.5° is formed by Bremsstrahlung radiation [67]. The missing Si(400) peak is only observed in normal Bragg–Brentano geometry at 69.1° [72]. In the inset image in Fig. 3, the one of the substrate peak at 53.6° (marked with a broken line) is also observed in the Py GIXRD patterns except for the film prepared at 1.5×10^{-3} mbar. This further supports the observed increase in porosity with Ar pressure in the TEM result shown in Fig. 1. In the inset image in Fig. 3, a slight shift of the Py(200) peak is observed at 5.0×10^{-3} mbar Ar pressure. This could be due to change of stress (which results in variation of lattice constant) in the sample or an instrumental error.

3.2. Magnetic hystereses of Py films as a function of Ar pressure

In Fig. 4(a) and (b), the in-plane and out-of-plane magnetic hysteresis loops of the continuous Py films prepared at varying Ar pressure are shown, respectively. From these VSM results, it is obvious that the saturation magnetization of the Py films decreases with the increase of Ar pressure. Relative values in comparison to the bulk Py saturation magnetization (860 kAm^{-1}) are shown in Table 1. The in-plane saturation field seen in Fig. 4(a) increases from 15 mT to more than 1200 mT with increasing Ar pressure. The out-of-plane saturation field decreases according to Fig. 4(b) from 1300 mT to 600 mT with increasing Ar pressure. The in-plane coercivity rapidly increases with increasing pressure from 0.12 mT at 1.5×10^{-3} mbar to 5.73 mT at 7.0×10^{-3} mbar, after which we observe a slight decrease to 4.30 mT at 30.0×10^{-3} mbar. This is specified in Table 1. Close-up views of the in-plane hysteresis loops showing change in coercivity and saturation field are provided in the Supplementary Material (Fig. S2).

3.3. Experimentally observed domain configurations as a function of Ar pressure

Fig. 5 shows MFM images of remanent domain configurations, i.e., zero-field states of the patterned Py films prepared at different Ar pressures. Nine out of two hundred squares patterned in an array are respectively shown. Magnetic domain images of a larger number of square patterned arrays are shown in the Supplementary Material (Fig. S3 to S5). Landau domains in Fig. 5(a), tulip domains in Fig. 5(b), irregular domains in Fig. 5(c) and no domain configurations in Fig. 5(d) are visible. The number of squares showing the Landau, tulip, diamond and irregular structures as remanent states were counted after each magnetization cycle. For the squares prepared at 1.5×10^{-3} mbar Ar pressure, approximately 90% of the squares show the Landau structure. The remaining squares show tulip or diamond configurations. For the squares prepared at 5.0×10^{-3} mbar Ar pressure, no square shows the Landau structure as the remanent state. However, approximately 60% of the squares show multiple tulip configurations at the corners as

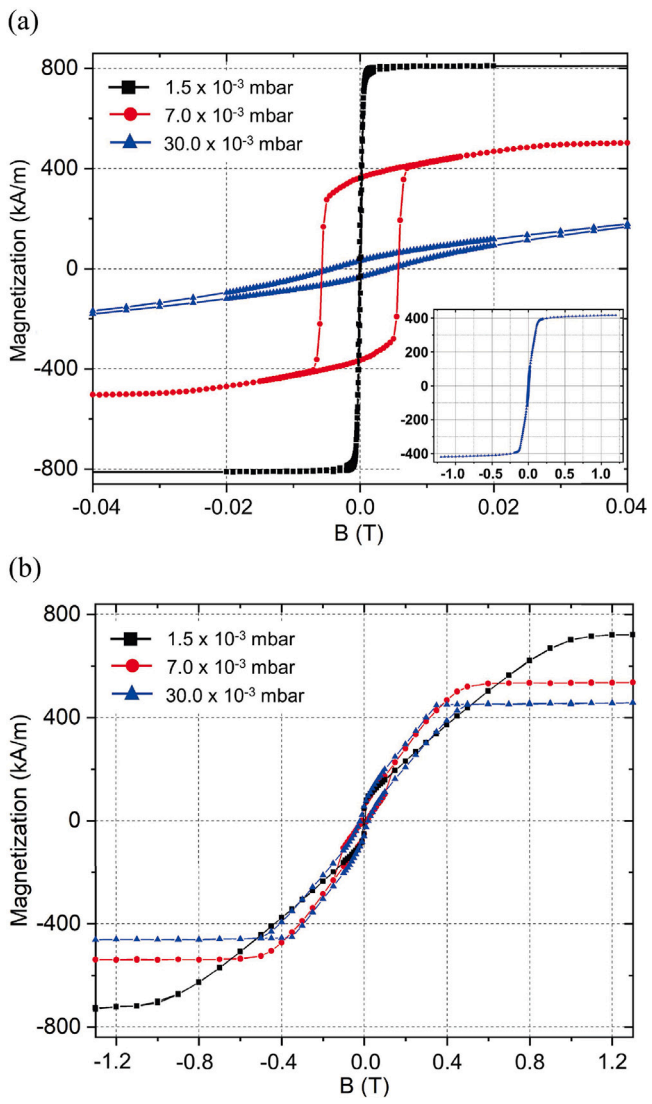

Fig. 4. In-plane (a) and out-of-plane (b) magnetic hysteresis loops of Py films prepared at different Ar pressures. The inset in (a) shows an in-plane hysteresis loop of the film prepared at 30.0×10^{-3} mbar Ar pressure. (a) With increasing sputter pressure, the field needed for in-plane saturation increases. (b) In contrast to the in-plane loop, with increasing sputter pressure the field needed for an out-of plane saturation decreases.

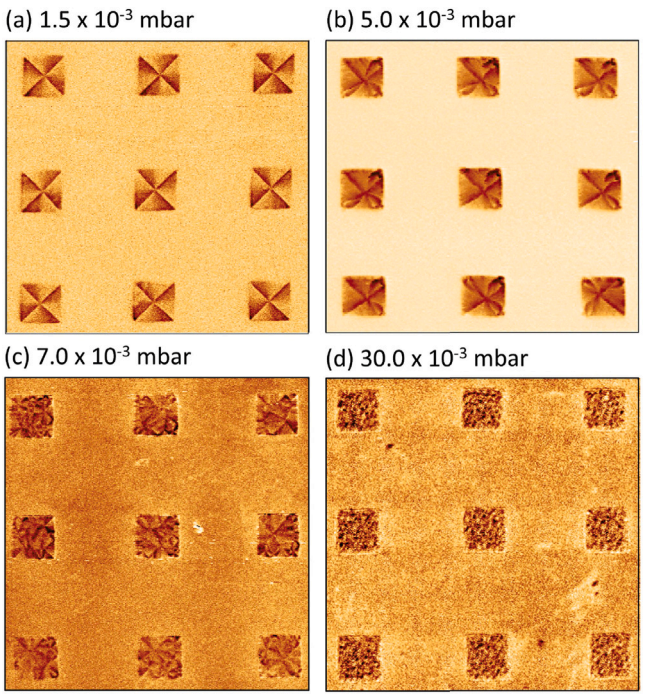

Fig. 5. MFM images in the remanent states of Py squares of 5 μm edge lengths and 10 μm edge-to-edge interdistance prepared at different Ar pressures. (a) At low sputter pressure, Landau patterns are reproducibly formed. (b) to (d) With increasing sputter pressure the domain structures become more irregular culminating into small irregular domains at high pressure.

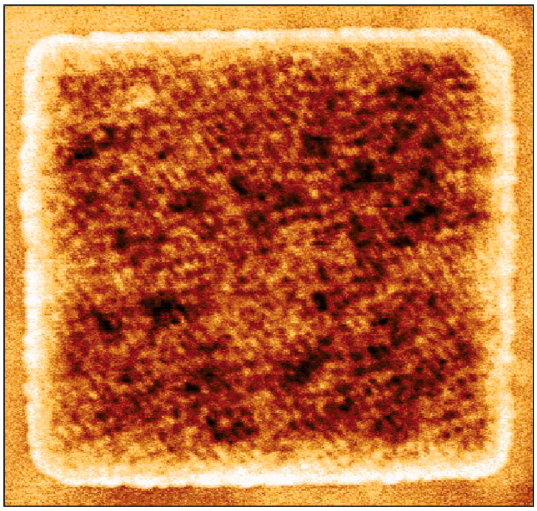

Fig. 6. A MFM image in the remanent state of a Py square of 5 μm edge length prepared at 30.0×10^{-3} mbar Ar pressure. A weak stripe domain pattern confirms the presence of a weak perpendicular anisotropy inside the film.

remanent states. For repeated cycles of magnetic field applied during MFM measurements, the positions of the tulip configurations with respect to the corners of the squares change. The remaining squares show irregular domains with complex arrangements of vortices and antivortices in their remanent state. For the squares prepared at 7.0×10^{-3} mbar Ar pressure, again no Landau domain configuration is observed, but more than 80% of the squares show irregular domains and the remaining squares show multiple tulip configurations at the corners. For the squares prepared at 30.0×10^{-3} mbar Ar pressure, initially no apparent domain configuration was observed at any applied field. However, a high resolution scan showed the formation of weak stripe domains [14,20,73] inside the samples as shown in Fig. 6. The half period of these weak stripe domains is approximately 75 nm which is roughly equal to the thickness (67 nm) of the film [20,73].

In order to understand the formation of the remanent domain configurations in squares prepared at different Ar pressures, their domain evolution in applied field was studied in more detail. For this purpose MFM images were taken in external fields between saturation and remanent states as shown in Figs. 7–9, respectively. Two squares from each array were respectively selected for the observations.

For the squares prepared at 1.5×10^{-3} mbar Ar pressure, upon reduction of the applied field from the saturation state in Fig. 7(a), well-defined S-state end domains [5,22] form at the edges as seen in Fig. 7(b). The S- and C-state are the domain configurations formed close to saturation where magnetization forms an 'S' and a 'C' shape configurations, respectively [5,22]. By further decreasing the field, the S-state end domains expand inside the squares as shown in Fig. 7(c) and (d). At 2.4 mT in Fig. 7(e), the S-state end domains in the right square evolve into a four-domain configuration with a vortex formed close to the upper edge of the square. In the left square, the S-state end domains evolve to form a domain wall close to the left edge of the

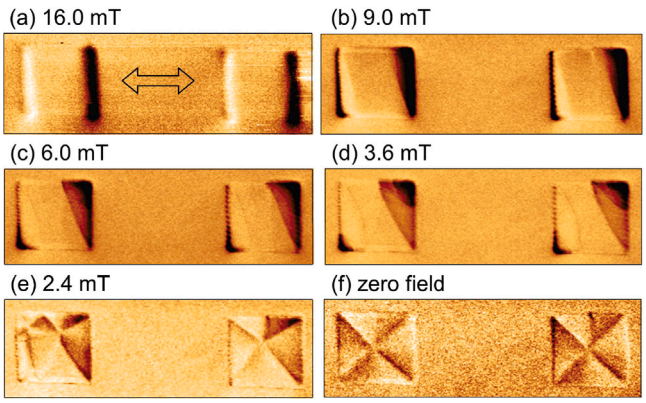

Fig. 7. MFM images of Py squares of 5 μm edge length and 65 nm thickness prepared at 1.5×10^{-3} mbar Ar pressure at different applied fields. The left–right arrow in (a) represents the direction of applied magnetic field. When the field is reduced, an S-state end domains start to form. These end domains expand into the element until at 2.4 mT a vortex is formed. At remanence the vortex moves to center of the square, resulting in a Landau pattern.

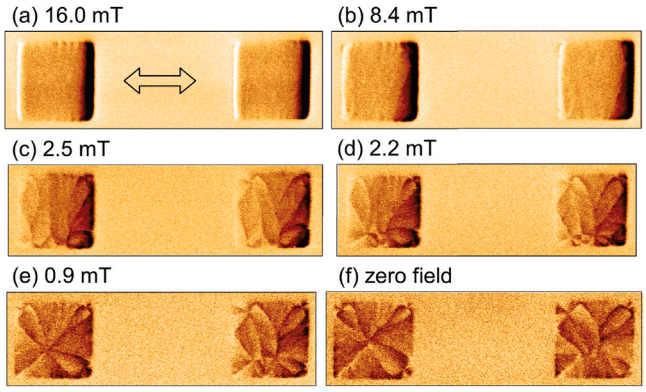

Fig. 8. MFM images of Py squares of 5 μm edge length and 50 nm thickness prepared at 5.0×10^{-3} mbar Ar pressure at different applied fields. The left–right arrow in (a) represents the direction of applied magnetic field. In contrast to the low Ar pressure sample of Fig. 7, the S-state end-domains do not appear when lowering the field. Instead multiple domains with vortices and antivortices are formed and the final state domain state is ill-defined.

square and a vortex close to the upper edge of the square. At vanishing external field, the domain wall formed close to the left edge of the left square is pushed out of the square, and the vortices formed close to the upper edges of both squares move towards the centers to form four domains inside the squares, as shown in Fig. 7(f). At zero field, the Landau domain configuration is established in both squares.

For the squares deposited at 5.0×10^{-3} mbar of Ar pressure and shown in Fig. 8, the well-defined S- or C-state end domains [5,22] are not formed. Upon reduction of the applied field from the saturation state in Fig. 8(a), multiple domain walls are nucleated starting at the edges as seen in Fig. 8(b) and (c). Upon further reduction of the field, multiple vortices and antivortices are nucleated within multiple tulip configurations at the corners of the squares, as shown in Fig. 8(d) to (f). The remanent configurations close to the corners of the squares differ from square to square.

For the squares deposited at 7.0×10^{-3} mbar of Ar pressure, the reduction of the applied field from saturation does again not result in the well-defined S- or C-state end domains, as seen in Fig. 9(a) to (c). Domain walls being primarily perpendicular to the applied field are nucleated as shown in Fig. 9(d) to (f). This explains the increase of remanent magnetization with increasing sputter pressure. The detailed

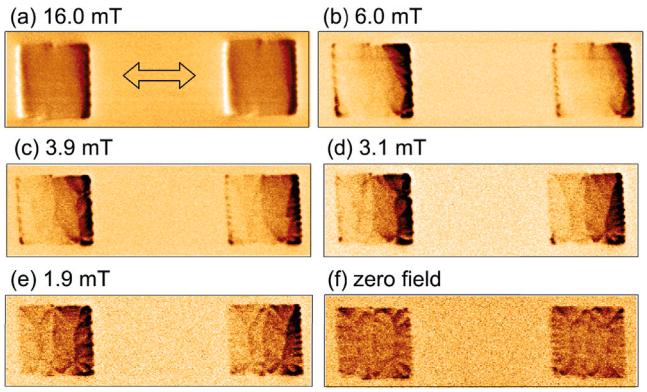

Fig. 9. MFM images of Py squares of 5 μm edge length and 51 nm thickness prepared at 7.0×10^{-3} mbar Ar pressure at different applied fields. The left–right arrow in (a) represents the direction of applied magnetic field. As in Fig. 8, many domains are nucleated, but they are aligned clearly perpendicular to the field direction.

magnetization configurations in the remanent states of the squares differ from each other.

3.4. Energies of zero-field domain configurations

In Fig. 10, out of many possible zero-field domain configurations, four experimentally relevant domain configurations calculated for a 60 nm thick 5 × 5 μm^2 Py film are shown. No grain morphology was assumed in the simulations. The Landau, tulip and irregular domain configurations were obtained by selecting a random magnetization configuration as an initial state. The diamond configuration was obtained from a seven-domains configuration initial state. For Landau and diamond configurations, the magnetization was allowed to relax according to the convergence criterion mentioned in Section 2. Whereas, for tulip and irregular configurations, simulations were terminated prior to convergence. Corresponding magnetic energies are also shown in Fig. 10. The Landau domain configuration has the lowest energy. The energy of the tulip configuration is higher because of the formation of an extra vortex and domain walls at the corner of the patterned film. The diamond domain configuration with multiple vortices and antivortices has an even higher energy. An irregular domain configuration as shown in Fig. 10(d) has the highest energy.

4. Discussion

From the TEM and GIXRD measurements shown in Figs. 1 and 3, respectively, and as well from the reduction of saturation magnetization in Table 1, it is clear that the morphology of the films changes from denser to more porous with possible oxidation with the increase of the Ar pressure. With decreasing film density, the exchange interactions between the grains of the polycrystalline films is expected to become weaker [27]. This in turn explains why the average size of the magnetic domains inside the squares decreases with increasing Ar pressure, as observed in Figs. 5 to 9. Moreover, the EDX data presented in Table 1 proves that the stoichiometry of films prepared at 1.5×10^{-3} mbar Ar pressure is closest to the target composition ($Ni_{80}Fe_{20}$). Thus, the magnetostriction coefficient of those films is the lowest [33,39]. Because of the relatively high density and low magnetostriction coefficient the lowest in-plane coercivity and in-plane saturation field are observed, as shown in Fig. 4(a). In this case, the magnetic domains inside the squares are solely defined by the shape of the squares rather than by the film morphology. This leads to the formation of well-defined end domains and the magnetization always evolves to the Landau domain configuration in the ground state, which is the lowest energy state for an ideal dense film having no granular

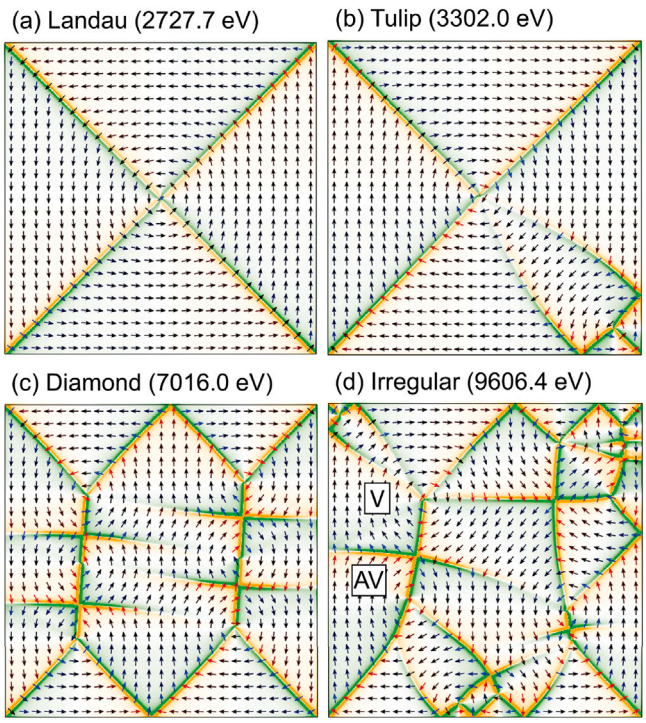

Fig. 10. OOMMF-simulated domain configurations of a 5 × 5 μm^2 and 60 nm thick Py square along with their calculated total magnetic energies. Locations of a vortex (V) and an antivortex (AV) are indicated in (d). Each arrow represents an averaged magnetization vector inside 20 × 20 adjacent cells on the sample surface. Black arrows represent in-plane magnetization, whereas blue and red arrows are the in-plane projections of magnetization vectors tilted upwards and downwards, respectively. Green and orange areas represent positive and negative charge densities, respectively. Only the lowest energy state of the Landau domain shown in (a) was observed in the sample prepared at 1.5×10^{-3} mbar. The non-equilibrium domains shown in (b) and (d) resemble the MFM images samples prepared at 5.0×10^{-3} and 7.0×10^{-3} mbar, respectively.

texture and internal stress, as seen in Section 3.4. For increasing Ar pressure, the film growth involves more and more columnar grains separated by voids. This inevitably results in an increase of pinning sites for the vortices, antivortices and domain walls [58–60]. Consequently, the in-plane coercivity and in-plane saturation field increase, as seen in Fig. 4(a). Moreover, the Ni content was found to increase when the Ar pressure increases. This is due to the reduced relative mean free path of the sputtered Fe atoms with respect to the Ni atoms [54,74]. The increase of Ni content and hence the magnetostriction coefficient of the film make magnetization sensitive to stress inside the film. As a result, irregular and smaller domains, especially at the sample edges, are formed because of the local variation of stress at the edges [10]. Therefore an increase of the complexity of the end domains is observed in Figs. 8 and 9. The increased number of pinning sites and the increase of magnetostriction coefficient of the film lead to a stabilization of multiple tulip configurations and irregular domains in remanent states, which are energetically less favorable for an ideal dense and stress-free film as seen in Section 3.4. The stress and inter-granular interactions inside the films prepared at higher Ar pressure induce energy barriers in the magnetic energy landscape and in consequence stabilize these local-minimum energy states. Moreover, local variations in the tulip and irregular domains configurations from one square to another one indicate that the remanent states in these cases are not well-defined. Films prepared at 30.0×10^{-3} mbar Ar pressure show an increase in O content at the voids in Fig. 2. This could be due to oxidation of the porous film exposed to the atmospheric oxygen as also reported by Refs. [75,76]. The EDX analysis in Table 1 confirms the increase of oxygen content with increasing Ar pressure.

An increase of perpendicular anisotropy with Ar pressure was found with the formation of weak stripe domains in the films prepared at 30.0×10^{-3} mbar, as shown in Fig. 6. The granular shape anisotropy induces perpendicular anisotropy inside those films prepared at relatively high Ar pressures [36,37]. The shape anisotropy calculated by assuming perfect non-interacting columnar grains [77] of 10 nm diameter for the film prepared at 30.0×10^{-3} mbar Ar pressure is 52 kJ m^{-3}. In contrast, the perpendicular anisotropy calculated from the out-of-plane hysteresis loop for this film is 6.4 kJ m^{-3}. The large difference between the anisotropy constants indicates a non-zero interaction between the grains. In addition, the stress-induced anisotropy also contributes to the perpendicular anisotropy of the film. However, the calculation of the strength and orientation of the stress-induced anisotropy is beyond the scope of the present investigations. Thus, a final conclusion about the interaction between columnar grains and contributions of stress-induced anisotropy to the total perpendicular anisotropy of the film is not yet advisable.

5. Conclusion

We investigated the relationship between the Ar sputter pressure and structural and magnetic properties of Py thin film elements with size of 5 × 5 μm^2 and a thickness of 60 ± 10 nm. Increasing the sputter pressure from 1.5×10^{-3} to 30.0×10^{-3} mbar does not significantly affect the crystal structure of Py thin films. However, the O content increased strongly from 10 to 38%, accompanied by a small increase in Ni content from 80 to 84%. From cross section TEM observations, we conclude that the increase in sputter pressure resulted in a reduction of film density. At 30.0×10^{-3} mbar, columnar grains separated by voids were formed. These changes in film composition and texture are accompanied by a reduction in saturation magnetization from 92 down to 53% of the bulk value and a strong increase in in-plane coercivity from 0.12 to 4.3 mT. The hysteresis loops of films prepared at higher sputter pressure show a higher saturation field for fields applied parallel to the film, and lower saturation field perpendicular to the film, suggesting that an intrinsic perpendicular anisotropy develops in the films. The hysteresis loops showed that with increasing sputter pressure the films became magnetically hard.

At a low Ar pressure of 1.5×10^{-3} mbar, the films were soft and the square shape of the element determined the remanent domain structure. When the field was reduced from saturation, S-state end domains formed until at 2.4 mT a vortex entered the element. At zero field that configuration relaxed to a Landau domain configuration which was consistently obtained amongst 90% of the observed elements. When the Ar pressure was increased above 5.0×10^{-3} mbar, the S-state end domain was no longer obtained. Instead many domains nucleated and tulip structures were formed as remanent domain structure. At 7.0×10^{-3} mbar the domains aligned perpendicular to the field and no tulip domains were found. At zero field irregular domain structures with sizes ~1 μm were formed. Since the micromagnetic simulations showed that the tulip and irregular domain structures are non-equilibrium states for an ideally dense film, this indicates that the domain configurations become increasingly dependent on grain structure at higher Ar pressures. The magnetically hard films prepared at 30.0×10^{-3} mbar showed weak stripe domains confirming the presence of perpendicular anisotropy in the films. These relationships between the deposition parameters, film grain structure, and magnetic properties offer guidelines for the realization of thin Py elements with well-defined and reproducible domain structures for use in magnetic sensors and spin-logic applications.

Declaration of competing interest

The authors declare that they have no known competing financial interests or personal relationships that could have appeared to influence the work reported in this paper.

Data availability

Data will be made available on request.

Acknowledgments

We thank Mr. Rudolf Karos (Leibniz Institute for New Materials, Saarbrücken) for the GIXRD measurements and Mr. Jörg Schmauch (Experimental Physics, Saarland University, Saarbrücken) for imaging of the cross-sections of the Py films by TEM and for the EDX measurements.

Appendix A. Supplementary data

Supplementary material related to this article can be found online at https://doi.org/10.1016/j.jmmm.2023.171138.

References

[1] F. Cheynis, A. Masseboeuf, O. Fruchart, N. Rougemaille, J.C. Toussaint, R. Belkhou, P. Bayle-Guillemaud, A. Marty, Controlled switching of Néel caps in flux-closure magnetic dots, Phys. Rev. Lett. 102 (10) (2009) 107201, http://dx.doi.org/10.1103/PhysRevLett.102.107201.

[2] P. Pirro, T. Koyama, T. Brächer, T. Sebastian, B. Leven, B. Hillebrands, Experimental observation of the interaction of propagating spin waves with Néel domain walls in a Landau domain structure, Appl. Phys. Lett. 106 (23) (2015) 232405, http://dx.doi.org/10.1063/1.4922396.

[3] B. Van Waeyenberge, A. Puzic, H. Stoll, K.W. Chou, T. Tyliszczak, R. Hertel, M. Fähnle, H. Brückl, K. Rott, G. Reiss, I. Neudecker, D. Weiss, C.H. Back, G. Schütz, Magnetic vortex core reversal by excitation with short bursts of an alternating field, Nature 444 (7118) (2006) 461–464, http://dx.doi.org/10.1038/nature05240.

[4] S. Goolaup, M. Ramu, C. Murapaka, W.S. Lew, Transverse domain wall profile for spin logic applications, Sci. Rep. 5 (1) (2015) 9603, http://dx.doi.org/10.1038/srep09603.

[5] S. Cherifi, R. Hertel, J. Kirschner, H. Wang, R. Belkhou, A. Locatelli, S. Heun, A. Pavlovska, E. Bauer, Virgin domain structures in mesoscopic Co patterns: Comparison between simulation and experiment, J. Appl. Phys. 98 (4) (2005) 043901, http://dx.doi.org/10.1063/1.2007872.

[6] J.W. Lau, M. Beleggia, M.A. Schofield, G.F. Neumark, Y. Zhu, Direct correlation of reversal rate dynamics to domain configurations in micron-sized permalloy elements, J. Appl. Phys. 97 (10) (2005) 10E702, http://dx.doi.org/10.1063/1.1851731.

[7] J.W. Lau, J.K. Bording, M. Beleggia, Y. Zhu, Energy barrier to magnetic vortex nucleation, Appl. Phys. Lett. 88 (1) (2006) 012508, http://dx.doi.org/10.1063/1.2150272.

[8] W. E, W. Ren, E. Vanden-Eijnden, Energy landscape and thermally activated switching of submicron-sized ferromagnetic elements, J. Appl. Phys. 93 (4) (2003) 2275–2282, http://dx.doi.org/10.1063/1.1536737.

[9] J.W. Lau, M. Beleggia, Y. Zhu, Common reversal mechanisms and correlation between transient domain states and field sweep rate in patterned permalloy structures, J. Appl. Phys. 102 (4) (2007) 043906, http://dx.doi.org/10.1063/1.2769779.

[10] J. McCord, Irregular domain patterns in structured magnetic thick films, J. Appl. Phys. 95 (11) (2004) 6855–6857, http://dx.doi.org/10.1063/1.1667833.

[11] S. Liou, R. Sabiryanov, S. Jaswal, J. Wu, Y. Yao, Magnetic domain patterns of rectangular and elliptic arrays of small permalloy elements, J. Magn. Magn. Mater. 226–230 (2001) 1270–1272, http://dx.doi.org/10.1016/S0304-8853(01)00073-7.

[12] I. Rissanen, L. Laurson, Coarsening dynamics of topological defects in thin permalloy films, Phys. Rev. B 94 (14) (2016) 144428, http://dx.doi.org/10.1103/PhysRevB.94.144428.

[13] G. Gubbiotti, L. Albini, G. Carlotti, M. De Crescenzi, E. Di Fabrizio, A. Gerardino, O. Donzelli, F. Nizzoli, H. Koo, R.D. Gomez, Finite size effects in patterned magnetic permalloy films, J. Appl. Phys. 87 (9) (2000) 5633–5635, http://dx.doi.org/10.1063/1.372473.

[14] S. Singh, H. Gao, U. Hartmann, Nucleation of stripe domains in thin ferromagnetic films, Phys. Rev. B 98 (2018) 060414, http://dx.doi.org/10.1103/PhysRevB.98.060414.

[15] D. Goll, G. Schütz, H. Kronmüller, Critical thickness for high-remanent single-domain configurations in square ferromagnetic thin platelets, Phys. Rev. B 67 (9) (2003) 094414, http://dx.doi.org/10.1103/PhysRevB.67.094414.

[16] C. Dietrich, R. Hertel, M. Huber, D. Weiss, R. Schäfer, J. Zweck, Influence of perpendicular magnetic fields on the domain structure of permalloy microstructures grown on thin membranes, Phys. Rev. B 77 (17) (2008) 174427, http://dx.doi.org/10.1103/PhysRevB.77.174427.

[17] T. Shinjo, T. Okuno, R. Hassdorf, K. Shigeto, T. Ono, Magnetic vortex core observation in circular dots of permalloy, Science 289 (5481) (2000) 930–932, http://dx.doi.org/10.1126/science.289.5481.930.

[18] H. Kronmüller, D. Goll, R. Hertel, G. Schütz, Critical thicknesses of domain formations in cubic particles and thin films, Phys. B 343 (1–4) (2004) 229–235, http://dx.doi.org/10.1016/j.physb.2003.08.099.

[19] A. Wachowiak, J. Wiebe, M. Bode, O. Pietzsch, M. Morgenstern, R. Wiesendanger, Direct observation of internal spin structure of magnetic vortex cores, Science 298 (5593) (2002) 577–580, http://dx.doi.org/10.1126/science.1075302.

[20] A. Hubert, R. Schäfer, Magnetic Domains : The Analysis of Magnetic Microstructures, Springer, Berlin, 1998, http://dx.doi.org/10.1007/978-3-540-85054-0.

[21] A. Hubert, M. Rührig, Micromagnetic analysis of thin-film elements (invited), J. Appl. Phys. 69 (8) (1991) 6072–6077, http://dx.doi.org/10.1063/1.347774.

[22] L.J. Heyderman, S. Czekaj, F. Nolting, E. Müller, P. Fischer, P. Gasser, L. López-Díaz, Photoemission electron microscopy study of remanent magnetic domain states in ferromagnetic wedge films deposited on substrates with micrometer-sized square plateaus, J. Appl. Phys. 99 (6) (2006) 063904, http://dx.doi.org/10.1063/1.2174119.

[23] W. Karboul-Trojet, Y. Roussigné, D. Faurie, S.M. Chérif, Static and dynamic study of magnetic properties in FeNi film on flexible substrate, effect of applied stresses, Eur. Phys. J. B 85 (10) (2012) 339, http://dx.doi.org/10.1140/epjb/e2012-30274-0.

[24] E. Feldtkelle, Review on domains in thin magnetic samples , J. Phys. Colloques 32 (C1) (1971) C1–452–C1–456, http://dx.doi.org/10.1051/jphyscol:19711154.

[25] M.T. Bryan, D. Atkinson, R.P. Cowburn, Experimental study of the influence of edge roughness on magnetization switching in permalloy nanostructures, Appl. Phys. Lett. 85 (16) (2004) 3510–3512, http://dx.doi.org/10.1063/1.1806566.

[26] Y.-T. Chen, J.-Y. Tseng, T.-S. Sheu, Y. Lin, S. Lin, Effect of grain size on magnetic properties and microstructure of Ni80Fe20 thin films, Thin Solid Films 544 (2013) 602–605, http://dx.doi.org/10.1016/j.tsf.2012.12.058.

[27] T. Schrefl, H. Schmidts, J. Fidler, H. Kronmüller, The role of exchange and dipolar coupling at grain boundaries in hard magnetic materials, J. Magn. Magn. Mater. 124 (3) (1993) 251–261, http://dx.doi.org/10.1016/0304-8853(93)90123-J.

[28] E.B. Park, S.-U. Jang, J.-H. Kim, S.-J. Kwon, Induced magnetic anisotropy and strain in permalloy films deposited under magnetic field, Thin Solid Films 520 (18) (2012) 5981–5984, http://dx.doi.org/10.1016/j.tsf.2012.04.077.

[29] F. Liorzou, B. Phelps, D. Atherton, Macroscopic models of magnetization, IEEE Trans. Magn. 36 (2) (2000) 418–428, http://dx.doi.org/10.1109/20.825802.

[30] J. Shi, S. Tehrani, M.R. Scheinfein, Geometry dependence of magnetization vortices in patterned submicron NiFe elements, Appl. Phys. Lett. 76 (18) (2000) 2588–2590, http://dx.doi.org/10.1063/1.126417.

[31] J. Shi, T. Zhu, S. Tehrani, Y. Zheng, J.-G. Zhu, Switching anomaly and magnetization vortices of 200åthick NiFeCo elements in one-micron patterned arrays, J. Magn. Magn. Mater. 198–199 (1999) 251–254, http://dx.doi.org/10.1016/S0304-8853(98)01097-X.

[32] B. Gehrmann, Nickel–iron alloys with special soft magnetic properties for specific applications, J. Magn. Magn. Mater. 290–291 (2005) 1419–1422, http://dx.doi.org/10.1016/j.jmmm.2004.11.504.

[33] E. Klokholm, J.A. Aboaf, The saturation magnetostriction of permalloy films, J. Appl. Phys. 52 (3) (1981) 2474–2476, http://dx.doi.org/10.1063/1.328971.

[34] R.M. Bozorth, The permalloy problem, Rev. Modern Phys. 25 (1) (1953) 42–48, http://dx.doi.org/10.1103/RevModPhys.25.42.

[35] R. Schäfer, Domains in 'extremely' soft magnetic materials, J. Magn. Magn. Mater. 215–216 (2000) 652–663, http://dx.doi.org/10.1016/S0304-8853(00)00252-3.

[36] N. Amos, R. Fernandez, R. Ikkawi, B. Lee, A. Lavrenov, A. Krichevsky, D. Litvinov, S. Khizroev, Magnetic force microscopy study of magnetic stripe domains in sputter deposited permalloy thin films, J. Appl. Phys. 103 (7) (2008) 07E732, http://dx.doi.org/10.1063/1.2835441.

[37] D.S. Lo, M.M. Hanson, Origin of stripe domains in Ni–Fe films, J. Appl. Phys. 38 (3) (1967) 1342–1343, http://dx.doi.org/10.1063/1.1709614.

[38] J. McCord, B. Erkartal, T. von Hofe, L. Kienle, E. Quandt, O. Roshchupkina, J. Grenzer, Revisiting magnetic stripe domains — anisotropy gradient and stripe asymmetry, J. Appl. Phys. 113 (7) (2013) 073903, http://dx.doi.org/10.1063/1.4792517.

[39] C.B. Hill, W.R. Hendren, R.M. Bowman, P.K. McGeehin, M.A. Gubbins, V.A. Venugopal, Whole wafer magnetostriction metrology for magnetic films and multilayers, Meas. Sci. Technol. 24 (4) (2013) 045601, http://dx.doi.org/10.1088/0957-0233/24/4/045601.

[40] S. Voltan, C. Cirillo, H.J. Snijders, K. Lahabi, A. García-Santiago, J.M. Hernández, C. Attanasio, J. Aarts, Emergence of the stripe-domain phase in patterned permalloy films, Phys. Rev. B 94 (2016) 094406, http://dx.doi.org/10.1103/PhysRevB.94.094406.

[41] U. Helmersson, M. Lattemann, J. Bohlmark, A.P. Ehiasarian, J.T. Gudmundsson, Ionized physical vapor deposition (IPVD): A review of technology and applications, Thin Solid Films 513 (1–2) (2006) 1–24, http://dx.doi.org/10.1016/j.tsf.2006.03.033.

[42] S.M. Rossnagel, Magnetron sputtering, J. Vac. Sci. Technol. A 38 (6) (2020) 060805, http://dx.doi.org/10.1116/6.0000594.
[43] J.T. Gudmundsson, Physics and technology of magnetron sputtering discharges, Plasma Sources. Sci. Technol. 29 (11) (2020) 113001, http://dx.doi.org/10.1088/1361-6595/abb7bd.
[44] S. Min, J.A. Bain, D.W. Greve, Control of stress and plasma-induced heating during dc magnetron sputtering of permalloy films for microelectromechanical systems, J. Appl. Phys. 91 (10) (2002) 6824, http://dx.doi.org/10.1063/1.1452659.
[45] A.S. Dzhumaliev, Y.V. Nikulin, Y.A. Filimonov, Deposition of NiFe(200) and NiFe(111) textured films onto Si/SiO2 substrates by DC magnetron sputtering, Phys. Solid State 58 (5) (2016) 1053–1057, http://dx.doi.org/10.1134/S1063783416050073.
[46] J.D. Freeman, Effect of deposition conditions on the properties of thin permalloy film, J. Vac. Sci. Technol. A: Vac. Surf. Films 9 (3) (1991) 421–425, http://dx.doi.org/10.1116/1.577425.
[47] M.M. Yang, J.A. Aboaf, Rf-diode sputtered permalloy film, J. Appl. Phys. 66 (8) (1989) 3734–3740, http://dx.doi.org/10.1063/1.344059.
[48] A. Svalov, B. González Asensio, A. Chlenova, P. Savin, A. Larrañaga, J. Gonzalez, G. Kurlyandskaya, Study of the effect of the deposition rate and seed layers on structure and magnetic properties of magnetron sputtered FeNi films, Vacuum 119 (2015) 245–249, http://dx.doi.org/10.1016/j.vacuum.2015.05.037.
[49] A. Svalov, G. Kurlyandskaya, B. González Asensio, J. Collantes, A. Larrañaga, Tuning the structure and magnetic softness of thin permalloy films by variations in the thickness of titanium seed layer, Mater. Lett. 152 (2015) 159–162, http://dx.doi.org/10.1016/j.matlet.2015.03.072.
[50] G. Nahrwold, J.M. Scholtyssek, S. Motl-Ziegler, O. Albrecht, U. Merkt, G. Meier, Structural, magnetic, and transport properties of permalloy for spintronic experiments, J. Appl. Phys. 108 (1) (2010) 013907, http://dx.doi.org/10.1063/1.3431384.
[51] X. Li, Z. Yang, Effects of sputtering conditions on the structure and magnetic properties of Ni–Fe films, Mater. Sci. Eng. B 106 (1) (2004) 41–45, http://dx.doi.org/10.1016/j.mseb.2003.07.003.
[52] X.-l. Tang, H. Su, H.-w. Zhang, Z.-y. Zhong, Y.-l. Jing, Improving the morphological and magnetic properties of permalloy films by adopting ultra-low-pressure sputtering, Thin Solid Films 550 (2014) 616–620, http://dx.doi.org/10.1016/j.tsf.2013.11.005.
[53] K. Yamamoto, M. Kitada, Magnetic and magnetoresistive properties of sputtered permalloy thin films, J. Mater. Sci.: Mater. Electron. 7 (6) (1996) 455–459, http://dx.doi.org/10.1007/BF00180786.
[54] A.V. Svalov, I.R. Aseguinolaza, A. Garcia-Arribas, I. Orue, J.M. Barandiaran, J. Alonso, M.L. FernÁndez-Gubieda, G.V. Kurlyandskaya, Structure and magnetic properties of thin permalloy films near the "transcritical" state, IEEE Trans. Magn. 46 (2) (2010) 333–336, http://dx.doi.org/10.1109/TMAG.2009.2032519.
[55] Y. Hoshi, E. Suzuki, Changes in angular distribution of incident sputtered particles in sputter deposition of iron films, J. Magn. Soc. Jpn. 18 (1994) S1, 323–326, http://dx.doi.org/10.3379/jmsjmag.18.S1_323.
[56] S. Mahieu, G. Buyle, D. Depla, S. Heirwegh, P. Ghekiere, R. De Gryse, Monte Carlo simulation of the transport of atoms in DC magnetron sputtering, Nucl. Instrum. Methods Phys. Res. B 243 (2) (2006) 313–319, http://dx.doi.org/10.1016/j.nimb.2005.09.018.
[57] S. Craig, G.L. Harding, Effects of argon pressure and substrate temperature on the structure and properties of sputtered copper films, J. Vac. Sci. Technol. 19 (2) (1981) 205–215, http://dx.doi.org/10.1116/1.571105.
[58] C. Holl, M. Knol, M. Pratzer, J. Chico, I.L. Fernandes, S. Lounis, M. Morgenstern, Probing the pinning strength of magnetic vortex cores with sub-nanometer resolution, Nature Commun. 11 (1) (2020) 2833, http://dx.doi.org/10.1038/s41467-020-16701-y.
[59] J. Trimble, J. Berezovsky, Barkhausen imaging: A magneto-optical approach to mapping the pinning landscape in soft ferromagnetic films, J. Magn. Magn. Mater. 523 (October 2020) (2021) 167585, http://dx.doi.org/10.1016/j.jmmm.2020.167585.
[60] A. Al-Qawasmeh, M.H. Badarneh, A. Obeidat, S. Abedrabbo, Surface roughness effects on magnetic properties of thin films: A computational Monte Carlo study, J. Magn. Magn. Mater. 562 (July) (2022) 169734, http://dx.doi.org/10.1016/j.jmmm.2022.169734.
[61] J. Crangle, G.M. Goodman, The magnetization of pure iron and nickel, Proc. R. Soc. Lond. Ser. A Math. Phys. Eng. Sci. 321 (1547) (1971) 477–491, http://dx.doi.org/10.1098/rspa.1971.0044.
[62] https://imagej.net/ij/index.html.
[63] M. Donahue, D. Porter, OOMMF User's Guide, Version 1.0, NISTIR 6376, National Institute of Standards and Technology, Gaithersburg, MD, 1999.
[64] K.M. Lebecki, D. Hinzke, U. Nowak, O. Chubykalo-Fesenko, Key role of temperature in ferromagnetic Bloch point simulations, Phys. Rev. B 86 (2012) 094409, http://dx.doi.org/10.1103/PhysRevB.86.094409.
[65] O. Šipr, S. Mankovsky, H. Ebert, Spin wave stiffness and exchange stiffness of doped permalloy via ab initio calculations, Phys. Rev. B 100 (2) (2019) 1–11, http://dx.doi.org/10.1103/PhysRevB.100.024435.
[66] G. Williamson, W. Hall, X-ray line broadening from filed aluminium and wolfram, Acta Metall. 1 (1) (1953) 22–31, http://dx.doi.org/10.1016/0001-6160(53)90006-6.
[67] R.A. Vaia, M.S. Weathers, W.A. Bassett, Anomalous peaks in grazing incidence thin film X-ray diffraction, Powder Differ. 9 (1) (1994) 44–49, http://dx.doi.org/10.1017/S0885715600019679.
[68] L.Y. Zhao, H. Jalili, N. Panjwani, T. Chan, Z.H. He, N.F. Heinig, K.T. Leung, Formation of ferromagnetic iron core-shell nanocubes on a H-terminated Si(100) surface by electrodeposition, Electrochem. Solid-State Lett. 10 (10) (2007) K47, http://dx.doi.org/10.1149/1.2759604.
[69] Y. Sohn, D. Pradhan, A. Radi, K.T. Leung, Interfacial electronic structure of gold nanoparticles on Si(100): Alloying versus quantum size effects, Langmuir 25 (2009) 9557–9563, http://dx.doi.org/10.1021/la900828v.
[70] D. Resnik, D. Vrtacnik, S. Amon, Morphological study of 311 crystal planes anisotropically etched in (100) silicon: role of etchants and etching parameters, J. Micromech. Microeng. 10 (3) (2000) 430, http://dx.doi.org/10.1088/0960-1317/10/3/319.
[71] L. Zhao, N. Heinig, K.T. Leung, Formation of Au–Pt alloy nanoparticles on a Si substrate by simple dip-coating at room temperature, Langmuir 29 (3) (2013) 927–931, http://dx.doi.org/10.1021/la303809m.
[72] P.A. Flinn, G.A. Waychunas, A new x-ray diffractometer design for thin-film texture, strain, and phase characterization, J. Vac. Sci. Technol. B 6 (1988) 1749, http://dx.doi.org/10.1116/1.584172.
[73] F. Virot, L. Favre, R. Hayn, M.D. Kuz'min, Theory of magnetic domains in uniaxial thin films, J. Phys. D: Appl. Phys. 45 (40) (2012) 405003, http://dx.doi.org/10.1088/0022-3727/45/40/405003.
[74] W. Zhang, W. Zhang, L. Lin, B. Peng, H. Jiang, S. Yang, Composition control and its influence to the magnetic properties of TbFex film, J. Magn. Magn. Mater. 280 (1) (2004) 143–146, http://dx.doi.org/10.1016/j.jmmm.2004.03.001.
[75] M. Salou, B. Lescop, S. Rioual, A. Lebon, J.B. Youssef, B. Rouvellou, Initial oxidation of polycrystalline permalloy surface, Surf. Sci. 602 (17) (2008) 2901–2906, http://dx.doi.org/10.1016/j.susc.2008.07.012.
[76] M.R. Fitzsimmons, T.J. Silva, T.M. Crawford, Surface oxidation of permalloy thin films, Phys. Rev. B 73 (1) (2006) 014420, http://dx.doi.org/10.1103/PhysRevB.73.014420.
[77] H. Fujiwara, An estimation of perpendicular anisotropy of magnetic thin films originating from non-magnetic grain boundaries, J. Phys. Soc. Japan 20 (11) (1965) 2092, http://dx.doi.org/10.1143/JPSJ.20.2092.